CSIRO PUBLISHING

International Journal of Wildland Fire **2021**, *30*, 197–214
https://doi.org/10.1071/WF20088

Quantifying merging fire behaviour phenomena using unmanned aerial vehicle technology

Alexander Filkov [A,B,C], *Brett Cirulis* [A] *and Trent Penman* [A]

[A]School of Ecosystem and Forest Sciences, University of Melbourne, Creswick, Vic. 3363, Australia.
[B]Bushfire and Natural Hazards Cooperative Research Centre, Melbourne, Vic. 3002, Australia.
[C]Corresponding author. Email: alexander.filkov@unimelb.edu.au

Abstract. Catastrophic wildfires are often a result of dynamic fire behaviours. They can cause rapid escalation of fire behaviour, increasing the danger to ground-based emergency personnel. To date, few studies have characterised merging fire behaviours outside the laboratory. The aim of this study was to develop a simple, fast and accurate method to track fire front propagation using emerging technologies to quantify merging fire behaviour at the field scale. Medium-scale field experiments were conducted during April 2019 on harvested wheat fields in western Victoria, Australia. An unmanned aerial vehicle was used to capture high-definition video imagery of fire propagation. Twenty-one junction and five inward parallel fire fronts were identified during the experiments. The rate of spread (ROS) of junction fire fronts was found to be at least 60% higher than head fire fronts. Thirty-eight per cent of junction fire fronts had increased ROS at the final stage of the merging process. Furthermore, the angle between two junction fire fronts did not change significantly in time for initial angles of 4–14°. All these results contrast with previous published work. Further investigation is required to explain the results as the relationship between fuel load, wind speed and scale is not known.

Keywords: automatic georeferencing, fast post-processing, field experiments, fire front propagation and tracking, merging fire fronts, operational and management application, remote measurements, UAV.

Received 10 June 2020, accepted 20 November 2020, published online 10 December 2020

Introduction

Extreme fire events (EFEs) (Tedim *et al.* 2018) have become more regular around the world. During the 2019–20 fire season, EFEs in Australia burnt almost 19 million ha, destroyed over 3000 houses, killed 33 people and were estimated to have killed more than 1 billion animals (Filkov *et al.* 2020*b*). EFEs create disproportionate risks to environmental and human assets as they can result in many casualties and loss of property. In most cases, these consequences are a result of dynamic fire behaviours (Viegas 2012; Filkov *et al.* 2018; Tedim *et al.* 2018; Filkov *et al.* 2020*a*).

One dynamic fire behaviour is merging fires (Viegas *et al.* 2012; Viegas *et al.* 2013; Thomas *et al.* 2017; Hilton *et al.* 2018; Raposo *et al.* 2018), which can lead to rapid increases in fire intensity and spread rate (Hilton *et al.* 2017). The convergence of separate individual fires into larger fires is known as coalescence and the merging of two lines of fire intersecting at an oblique angle is termed junction fire or junction fire fronts (Viegas *et al.* 2012). Fire coalescence, inward parallel fire fronts and junction fire fronts are all examples of merging fire fronts (Fig. 1). Fire coalescence and junction fire fronts behave in a manner that can defy suppression efforts even in the most prepared and equipped regions (Williams and Hamilton 2005). Erratic behaviour and difficulties in suppression allow fires to burn more intensely over larger areas, increasing the likelihood of loss of life, property and other assets.

Merging fire fronts have been recorded in several significant bushfires. For example, in the 2003 Canberra fires, the McIntyre's Hut and Bendora fires merged in the early afternoon (Doogan 2006). The merging fire apex *P* (Fig. 1*b*) spread rapidly and developed into an extremely destructive junction fire that resulted in four deaths, many injuries and property losses valued at AU$600 million to AU$1 billion.

Junction fire fronts have generally been studied experimentally at the metre scale (Viegas *et al.* 2012; Viegas *et al.* 2013; Raposo *et al.* 2018; Sullivan *et al.* 2019) with only one exception (Raposo *et al.* 2018), where the authors conducted three field experiments (47, 52 and 75 m). During laboratory and field experiments, researchers varied the angle between two fire fronts (θ) (Viegas *et al.* 2012), slope of the fuel bed, fuel type (Viegas *et al.* 2013; Raposo *et al.* 2018) and wind conditions (Sullivan *et al.* 2019).

There is a strong relationship between the velocity of the intersect point and the angle between the fire lines (Viegas *et al.* 2012). The non-dimensional form of the rate of spread R' of the intersect point of two oblique fire fronts (junction fire fronts) appears in Eqn 1 (Viegas *et al.* 2012).

$$R' = \frac{R_p}{R_0} \quad (1)$$

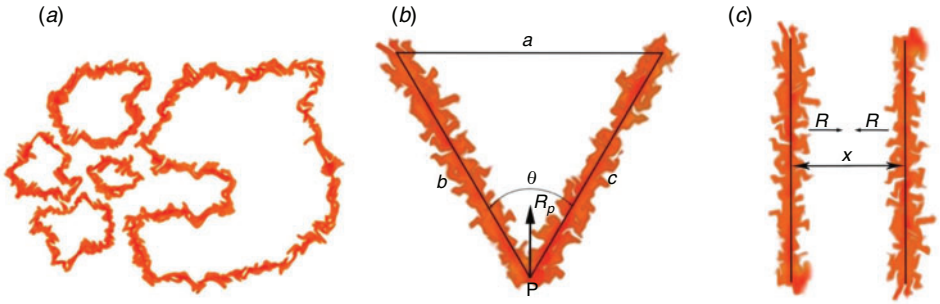

Fig. 1. Merging fire fronts: (*a*) fire coalescence; (*b*) junction fire fronts; (*c*) inward parallel fire fronts, where *a* is the maximum distance between the junction fire fronts and *b*, *c* are the lengths of the junction fire fronts; θ is the angle between junction fire fronts; R_P is the rate of spread of the intersect point of two junction fire fronts; *x* is the distance between parallel fire fronts; *R* is the rate of spread of parallel fire fronts.

R_P is the rate of spread of the intersect point of two junction fire fronts; R_0 is the basic rate of spread of a linear fire front in the same fuel bed in no-wind and no-slope conditions.

Two stages of junction fire development have been identified (Viegas *et al.* 2013; Raposo *et al.* 2018): an acceleration phase where the apex rate of spread (R_P) greatly increases at the start of the fire and a deceleration phase where the apex slows down and the fire extinguishes. In the deceleration phase, the fire behaves like a linear fire front. Viegas *et al.* (2013) argued that slope increases the distance travelled by the intersect point in the acceleration phase and changes in fuel bed composition have no effect on the non-dimensional rate of spread R'.

Fires may be classified as buoyancy-dominated or wind-dominated (Morvan and Frangieh 2018). Typically, buoyancy-driven fires are thought to propagate largely by radiation because most of the hot gases move upwards, and wind-driven fires largely by convection because the hot gases are pushed forward (Morvan and Frangieh 2018). Sullivan *et al.* (2019) conducted a series of 1-m-scale experiments in the absence and presence of wind to study its influence on apex velocity. In their study, they developed and introduced the so-called null hypothesis (Eqn 2):

$$R' = \frac{R_p}{R_0} = \frac{1}{\sin(\theta/2)} = \mathrm{cosec}\left(\frac{\theta}{2}\right), R_0 = R_l(no\ wind),$$
$$R_0 = R_l \sin\left(\frac{\theta}{2}\right)(wind) \quad (2)$$

where θ is the angle between junction fire fronts and R_l is the rate of spread of the linear fire front. They proposed an original approach to obtain the basic rate of spread R_0 for windy conditions. It was calculated as the rate of spread of the linear fire front (ignition line) R_l perpendicular to the wind and corrected to compensate for the effect of the different junction angles on each R_0. This was done by multiplying the rate of spread of the linear fire front R_l by the sine of half of each angle between junction fire fronts (Eqn 2).

This hypothesis assumes junction fire fronts merge under quasi-steady conditions and is a reasonable null hypothesis for no-wind conditions. Other researchers found no evidence that R' was enhanced over the null hypothesis for no-wind conditions, but found increases in R' for wind-driven conditions (Viegas *et al.* 2012, 2013; Raposo *et al.* 2018). This discrepancy was attributed to the different scale of the experiments, fuel load and fuel type (dense eucalyptus litter), and possibly fuel configuration that permitted a fire upstream of the ignition line. However, the mechanisms of heat transfer were not measured or analysed in any of these studies.

Physics-based modelling can be a powerful instrument to uncover physical phenomena beyond experimental limitations. Recently, Thomas *et al.* (2017) tested similar junction angles θ to Viegas *et al.* (2012) using the coupled atmosphere–fire model WRF-Fire (Coen *et al.* 2013), but at a larger scale: each simulated fire line was 1000 m long. They found that, in addition to the bulk fire-induced surface flow, sets of counter-rotating pairs of vertical vortices lying on or ahead of the fire lines of the junction fires were formed, and these vortices produced local acceleration of the fire front. However, they concluded that the vortical structures were not well resolved at the 20-m resolution used and were likely too small to be properly resolved by their simulations. Thomas *et al.* (2017) found some quantitative differences in the acceleration of the apex with the results of Viegas *et al.* (2012). The lack of agreement could be attributed to a scaling problem. For instance, laboratory experiments for low angles of junction fire fronts cannot capture all effects due to the small scale (Raposo *et al.* 2018).

Although physics-based models are the best instrument to provide insights into different phenomena, they are too slow and complex for operational purposes. Analytical and simplified models take seconds to minutes to produce a prediction including basic wind effects, compared with hours to days for a full physical model (Frangieh *et al.* 2018). The first simple analytical model based on energy concentration between the two arms of the junction was proposed by Viegas *et al.* (2012). It had considerable limitations, such as no slope or wind gradients. Hilton *et al.* (2018) developed a simplified model of the wind fields around wildfires based on a two-dimensional 'pyrogenic' potential flow formulation. When coupled to a wildfire perimeter propagation model, this can replicate basic wildfire interaction effects including fire line attraction, the shape of fire fronts and the enhanced coalescence of spot fires (Hilton *et al.* 2017). However, the model assumes that the plume is not significantly affected by the wind. It is therefore likely that the model can only be applied under certain conditions and further work is needed to

explore the experimental parameter space and extend the model for wind-driven conditions. The authors concluded that despite the good match to experimental results, the model should take flame attachment into account and it is likely that the model only applies under certain conditions that have not been fully explored in the experimental parameter space.

Extensive high temporal and spatial resolution experimental data at larger scales are required to fully understand how a given fire will merge and spread. Unmanned aerial vehicles (UAVs or drones) may be a useful tool in obtaining these measurements. In the last decade, they have been well utilised in the study of wildfires (Merino *et al.* 2012; Hua and Shao 2017; Fernández-Guisuraga *et al.* 2018). UAVs have been used for fire detection and monitoring (Hua and Shao 2017; Moran *et al.* 2019), fire management (Merino *et al.* 2012) and post-fire monitoring (Fernández-Guisuraga *et al.* 2018). They can be equipped with various sensing instruments, ranging from optical sensors (including visible and infrared) to microwave sensors (radar and LiDAR). Owing to flexibility, low cost and high-resolution data collection, rotary-wing drone remote sensing can fill data gaps about different fire behaviour phenomena.

The aims of the present study were:

- to develop a simple, fast and accurate method to track fire front propagation using UAVs,
- to quantitatively characterise fire behaviour of merging fires, and
- to compare fire behaviour characteristics with previous studies.

Methods

Study area and equipment

The study was conducted on agricultural lands in western Victoria, Australia (Fig. 2*a*). Small- and medium-scale field experiments were conducted between 1503 and 1620 hours on 12 April 2019 near Kingston, 110 km west of Melbourne. Two harvested wheat fields were used as experimental plots, as they form fairly homogeneous fuel beds. Fuel height varied from 18 to 30 cm in each plot and fuel load and moisture content were 1.1 ± 0.15 tonnes ha^{-1} (t ha^{-1}) (0.11 kg m^{-2}) and $11.9 \pm 2\%$ respectively. Fuel (straw) bed density and surface area-to-volume ratio were 0.46 ± 0.08 kg m^{-3} and 2240 ± 185 m^{-1} respectively. A drip torch (50% diesel fuel to 50% petrol) was used to progressively ignite lines of fuel in parallel, starting at the downwind edge of the plot (Fig. 2*b*). For each plot, the downwind line was ignited first, IL1 or IL4 respectively, and allowed to fully spread downwind to a fuel break and self-extinguish. Then, the next ignition line in the upwind direction (IL2 or IL5) was ignited and allowed to spread and self-extinguish. Finally, the last ignition line on the plot was ignited (IL3 or IL6). A total of six straight ignition lines (IL1–IL6) between 400 and 480 m long were ignited during the experiment.

An automatic weather station (AWS, 30-min temporal resolution) and two 2-dimensional DS-2 sonic sensors (Decagon Devices, Inc.) were used for air temperature, relative humidity, wind direction and speed measurements. The Ballarat Aerodrome AWS (no. 89002) is located 21 km south-east from the plots (−37.5127, 143.7911). Locations of the sonic sensors

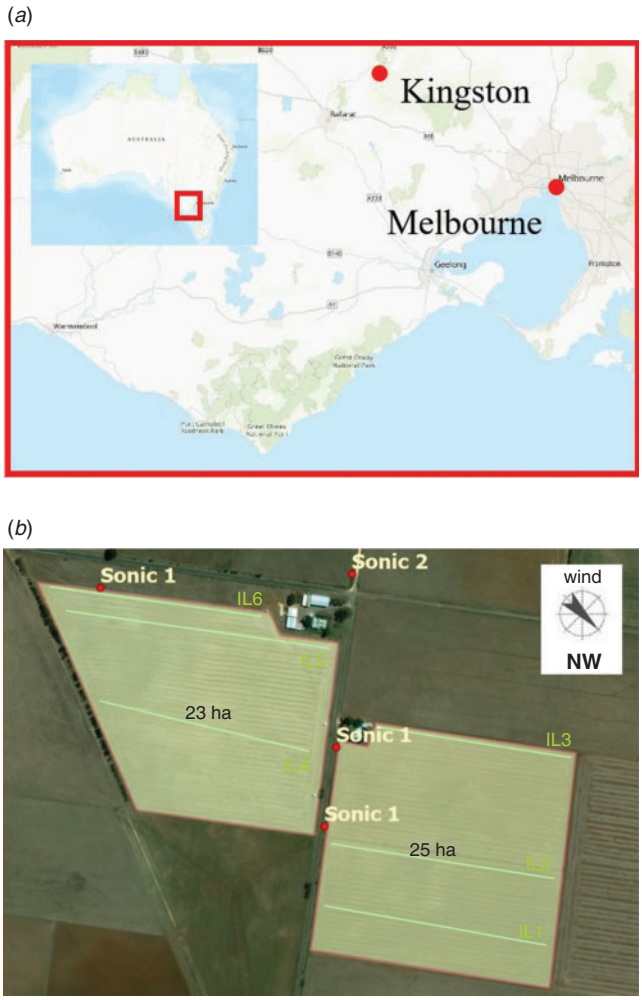

Fig. 2. (*a*) Geographical location of experimental plots. (*b*) Position of sonic sensors and ignition lines on the plots. Plot 1 is on the right and Plot 2 is on the left. Green lines represent ignition lines (IL1–IL6) and red dots represent sonic sensors.

are shown on Fig. 2*b*. One sonic sensor (Sonic 1, Fig. 2*b*) was repositioned during the study based on ignition location. Another sensor (Sonic 2) was used as a control sensor and remained in the same location during all tests. Air temperature and relative humidity were 20.5 ± 0.3°C and $22.8 \pm 2\%$ respectively. Wind direction data were taken from the AWS owing to the direction component of the sonic sensors malfunctioning. Wind direction (direction from which wind originates) was northerly at the beginning of the experiment, switching to north–north-westerly at the end. Wind speed was measured every minute 1.5 m above ground and was in the range 1.8–7.0 m s^{-1} (Fig. 3) with an average speed of 3.6 and 4.7 m s^{-1} for Sonic 1 and 2 respectively. It was not possible to analyse the influence of wind on merging fires owing to short duration of the merging process (less than 1 min) and coarse temporal resolution (1 min) of the sonic sensors. The slope was less than 5° at all plots.

A DJI Mavic Pro UAV was used to capture high-definition video imagery of fire propagation in synchrony with sensor data from the on-board global positioning system (GPS) and inertial

measurement unit (IMU). These sensors enabled the platform/camera orientation and position in space to be aligned with the video footage and the fire propagation georeferenced in GIS (geographic information system) software.

Data capture and processing

Video data were captured using the onboard camera on the DJI Mavic Pro. To minimise the georeferencing error of the final imagery, a stationary flight with an altitude of 30 m and a 90° camera angle (looking straight down) was maintained for each junction fire while video footage was recorded. Video was recorded at 1080p (1920 × 1080 pixels) resolution at 60 frames per second (fps). The CIRRUAS application (CompassDrone, Denver, CO, USA) was used with an android phone to record the necessary flight metadata for post processing. For each video footage, a CSV file was produced with the following metadata: UNIX time stamp, platform heading angle, platform pitch angle, platform roll angle, sensor latitude, sensor longitude, sensor true altitude, sensor horizontal field of view, sensor vertical field of view, sensor relative azimuth angle, sensor relative elevation angle, sensor relative roll angle. The post-processing phase was completed for each video and metadata files using the Full Motion Video (FMV) toolbox (Fig. 4*a*) within the *ArcGIS Pro* software (Macdonald 2017).

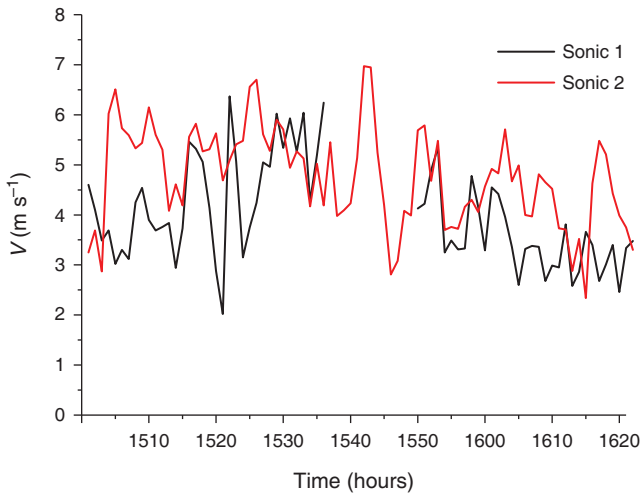

Fig. 3. Wind speed *V* during experiments. Data for Sonic 1 between 37 and 49 min are absent owing to relocation of the sensor between plots.

The video file was converted into an FMV-compliant format (georeferenced) before analysing the video footage. The metadata file containing sensor information is combined with the video file in a process called Multiplexing (Fig. 4*b*). The result is a video file with each frame georeferenced (Fig. 5, bottom window). Once it is multiplexed, the georeferenced frame of the filmed area appears on the map (Fig. 5, top window). The frame had a trapezium shape with dimensions of 100 m (top) × 110 m (base) × 60 m (sides). The multiplexed video file was then used to identify and spatially define fire fronts at set time intervals. The process of multiplexing takes ~3 min for each minute of video (Intel i7 CPU, 32 Gb RAM).

After the ignition line was started, the fire front produced fire tongues (Fig. 5, bottom window). Fire lines of two neighbouring tongues naturally merged together were identified as junction fire fronts and the angle between them as the initial angle. Parallel fire fronts were identified as two fire tongues burning parallel to each other.

We measured the travelling distance of the intersect point *P* (Fig. 1*b*) every 2 s to calculate rate of spread (ROS) of junction fire fronts. To calculate the angle between junction fire fronts, we used the law of cosines $\theta = \arccos((c^2 + b^2 - a^2)/2bc)$, where

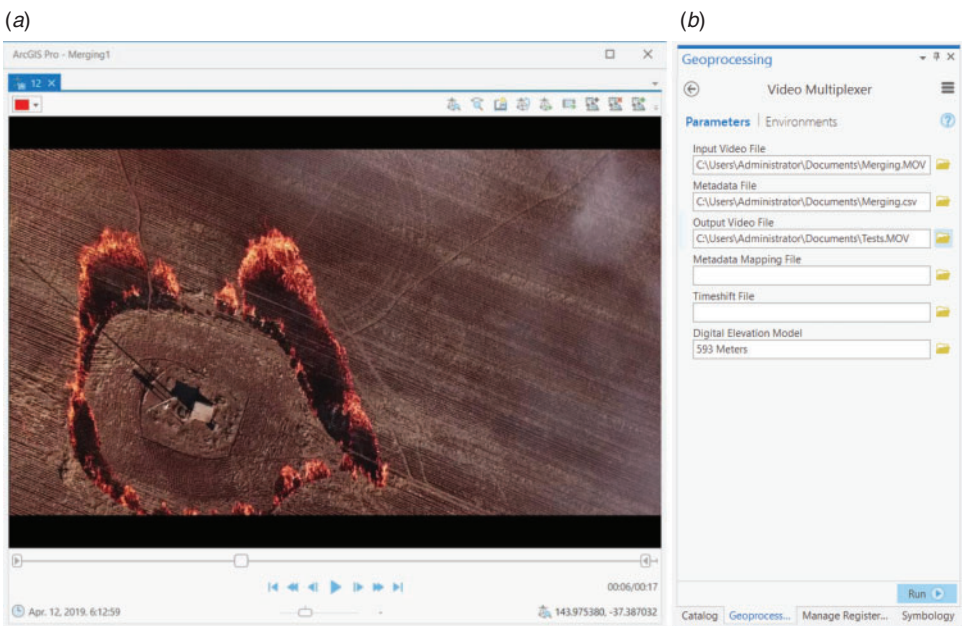

Fig. 4. Data georeferencing: (*a*) Full Motion Video toolbox in *ArcGIS Pro* software; (*b*) video multiplexer.

a, b and c are the sides of the triangle. To use this formula, we measured the length of all three sides of the triangle. Junction fire front lengths were determined as sides b and c of the triangle (Fig. 1*b*). Three points on the fire fronts were selected for each time step in the FMV toolbox using the *Add graphics* tool (Fig. 6*a*). One point was an intersect of two junction fire fronts (intersect point P) and two others were the points on each fire line. Once a point is selected, it automatically appears on the *ArcGIS Pro* map (Fig. 6*b*). The *Save video graphics* tool was then used to save created points in the *ArcGIS Pro* project. For better representation of fire progression, the selected points and merging fire lines were highlighted with different colours. Using the *ArcGIS Pro Measure* tool, the distance between selected points and the travelling distance of the intersect point were measured. Measurements of the sides of the triangle (a, b, c) and the travelling distance of intersect point P for each time step of 21 junction fires took ~3 h.

All parallel fire fronts observed during the experiments were approaching each other (i.e. inward parallel fire fronts). One point was selected on each fire front (left and right fire fronts hereafter) along the same convergence plane. After 5 s of spread, a second point was placed on each fire front and the distance between point pairs was measured. ROS could then be calculated for each fire front, left and right.

The non-dimensional form of the rate of spread R' described in Eqn 2 was used to compare ROS between different phenomena and with other studies. All the experiments were conducted in windy conditions. As such, it is important to describe the approach used to determine the basic ROS in our work. First, we determined the ROS of the linear fire front R_l – the ROS of the closest head fire to junction or parallel fire fronts. Basic ROS R_0 was then calculated following the method used by Sullivan *et al.* (2019), where the ROS of the linear fire front is corrected to compensate for the effect of the different oblique angles on R_0 ($R_0 = R_l \sin(\theta/2)$). The angle between the linear fire front and wind direction varied in the range 35–80°.

The ROS of the linear fire front R_l was measured in the vicinity of each junction and parallel fire fronts every 2 and 5 s respectively for their entire duration. Different time intervals were chosen owing to the significant difference in duration of selected phenomena. Ambient wind conditions were similar for each pair of linear fire front and junction fire front, linear fire front and parallel fire front as they were at close proximity to each other and measured at the same time.

All measurements were done in the area surrounded by the trapezium frame with the longest base of 110 m (Fig. 5) and after 30 s from ignition to avoid the build-up phase influencing the results (Cheney and Gould 1997). A head fire takes time to reach equilibrium or steady-state ROS after ignition; this process has been referred as the fire growth or build-up (Cheney and Gould 1997). Cheney *et al.* (1993) found that line fires in grasslands appeared to reach a quasi-steady speed across small plots (100 × 100 m) after ~15 s for ignition lines that were nominally 50 m long.

A linear regression analysis was conducted for quantitative estimations. Specifically, we calculated the slope of the regression line m, adjusted R^2 and significance value P. Response variables were the ROS of the intersect point of two junction fire fronts R_P and the angle θ between junction fire fronts. The predictor variable was time. Negative and positive relationships are indicated as decreasing and increasing trends (slopes) respectively. Owing to the different duration of each merging

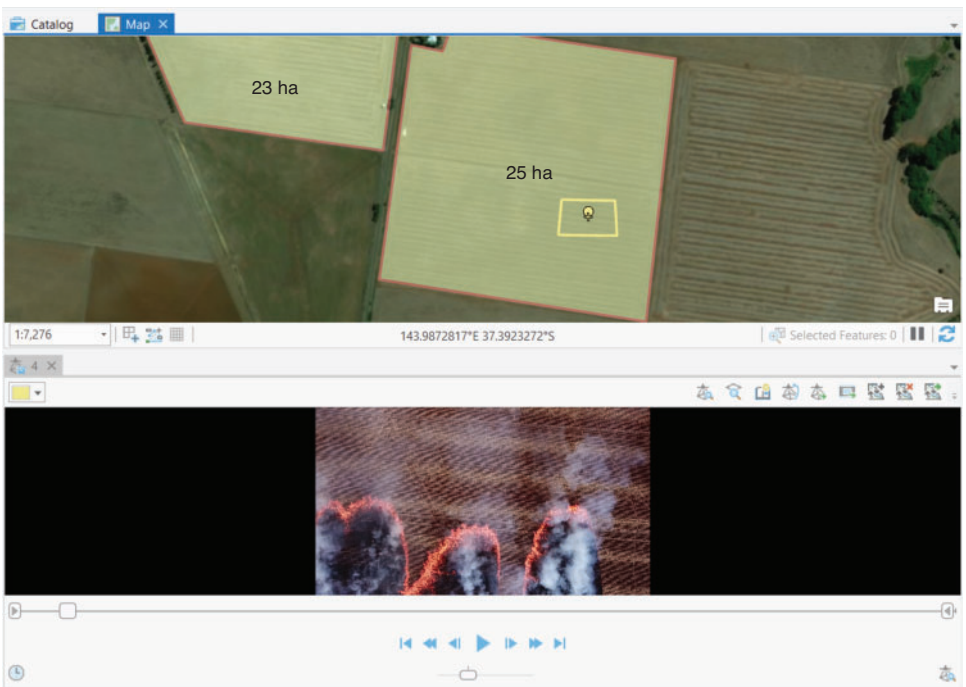

Fig. 5. Multiplexed video file. Top window shows a yellow trapezium frame of georeferenced filmed area on the map. Bottom window shows an original video frame.

(*a*)

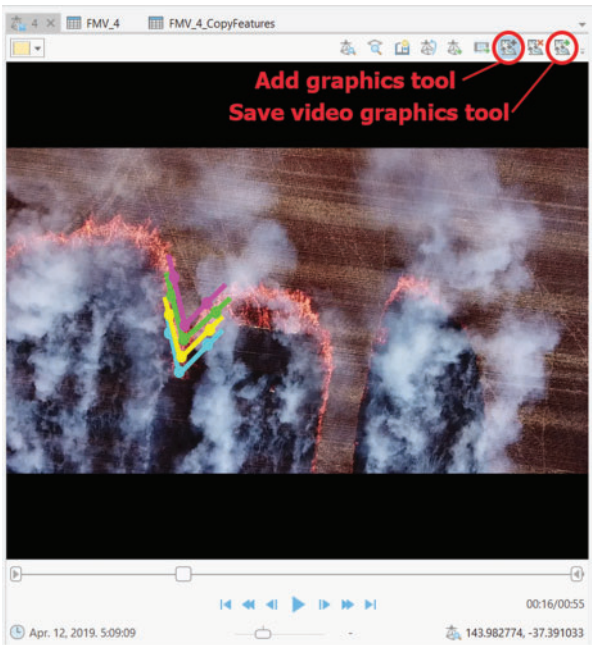

(*b*)

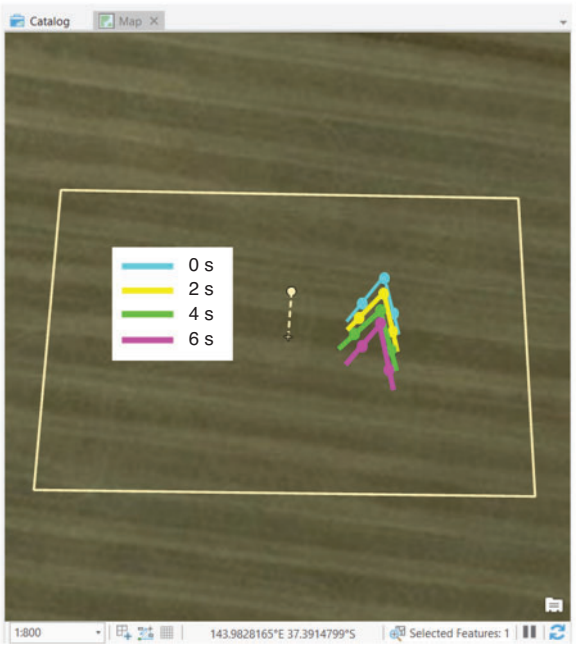

Fig. 6. Screen capture of the *ArcGIS Pro* interface: (*a*) Full Motion Video toolbox with selected tools; (*b*) georeferenced video. Each angle outlines the intersection of two fire lines. Colour represents location of a fire front at different time steps.

fire, we converted time steps to percentages of the final time. Initial time is the time when two fire tongues naturally merged together. Final time for R_P is the last time the angle between junction fire fronts became 180°. The final time for θ is one timestep prior to the last time.

In order to test the hypothesis that the ROS of merging fire fronts is statistically different from linear fire fronts, a one-way ANOVA was performed. Parallel fire fronts were excluded from the analysis as the assumption of homogeneity was not satisfied and the group sizes were not equal. Prior to conducting the ANOVA, the assumption of normality was evaluated using a Shapiro–Wilk test at the 0.05 level and was determined to be satisfied as the junction and linear fire fronts P values were 0.07 and 0.56 respectively. Furthermore, the assumption of homogeneity of variances was tested and satisfied based on Lavene's F test ($F = 3.35$, $P = 0.07$).

Results

Eleven videos were filmed during experiments and post processed (Fig. 7*a*). Twenty-six merging fire fronts were identified: 21 junction fire fronts and 5 parallel fire fronts (Fig. 7*b*) (Appendix 1, Tables A1–A4).

The junction fire fronts identified were separated into four groups depending on the recorded initial angle between oblique fire fronts θ_{in}: 4–14°, 28–34°, 40–59° and 77°. The highest number of fires (43%) were observed in the 28–34° group.

The ROS of junction, linear and parallel fire fronts was calculated as an average of all 2- and 5-s time intervals (Fig. 8). The mean ROS of junction fire fronts (1.75 m s^{-1}, s.d. 0.66) was 1.6 times higher than for linear (1.11 m s^{-1}, s.d. 0.34) and at least 20 times higher than for parallel (0.08 m s^{-1}, s.d. 0.05) fire fronts. Acute-angle (<14°) ROS of junction fire fronts was greater by 3–6 times than the linear fire front ROS. The independent between-groups ANOVA indicated that the mean ROS for the junction fire fronts was significantly different than the linear fire fronts, $F = 18.36$, $P = 9.8 \times 10^{-5}$. Thus, the null hypothesis of no differences between the means was rejected.

Comparisons of ROS and the angle between junction fire fronts θ are presented on Figs 9 and 10. ROS increased as the initial angle decreased (Fig. 9). The mean ROS was 1.02 m s^{-1} (s.d. 0.19), 1.49 m s^{-1} (s.d. 0.65), 1.49 m s^{-1} (s.d. 0.44) and 3.44 m s^{-1} (s.d. 1.81) for the initial angles 77°, 40–59°, 28–34° and 4–14° respectively. We found 38% of junction fire fronts exhibited an increase in ROS at the final stage of the merging process. Linear regression analysis showed that at the 0.05 level, the slope is not significantly different from zero for all initial angles (Fig. 9). This suggests that junction fire fronts do not notably change ROS during the merging process. However, this suggestion requires further investigation as the dataset is limited.

The angle between fire fronts did not increase significantly over time ($m = 0.05$, $P = 0.228$) (Fig. 10) for two oblique fire fronts with initial angles (θ_{in}) 4–14°. However, for the initial angles 28–34°, 40–59° and 77°, the slope of the regression line was between 0.3 and 0.4 and was statistically significant ($P < 0.035$).

Mean ROS of parallel fire fronts was 0.07 m s^{-1}, varying between 0.001 and 0.33 m s^{-1} (Fig. 11). ROS increases as fire lines come closer to each other. Faster ROS of the right fire line was observed during the experiments. It can be assumed that because the developed parallel fire fronts were not perfectly aligned with the wind direction (not possible in the field experiments), the resulting ROS was different for the left and right fire lines. It is supposed that small fluctuations of the ROS related to change in the wind speed (Fig. 3) rather than fire itself.

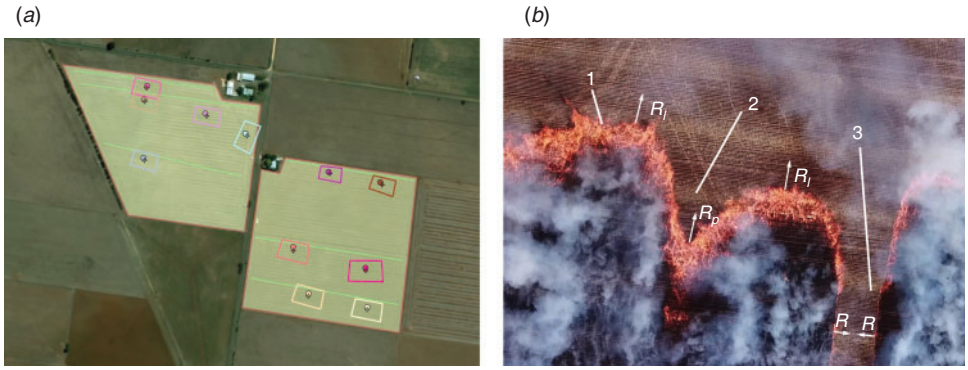

Fig. 7. (*a*) Bird's eye view of video footages. Each rectangle represents separate video footage. (*b*) Observed fires: (1) linear fire front; (2) junction fire fronts; (3) parallel fire fronts. R_P is the rate of spread of the intersect point of two junction fire fronts, R_l is the rate of spread of the linear fire front, R is the rate of spread of parallel fire fronts.

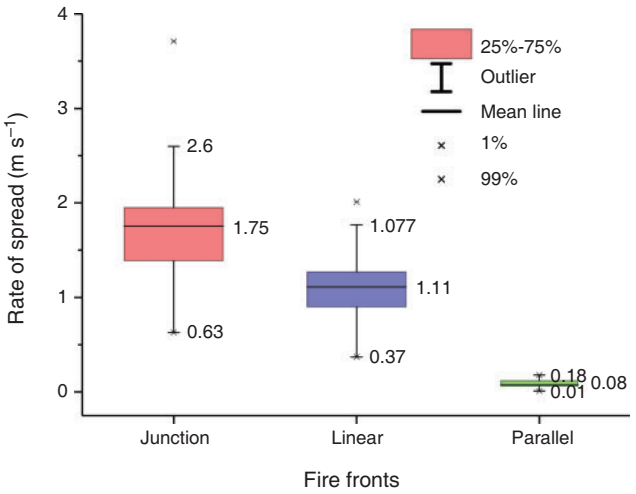

Fig. 8. Comparison of different types of fire front propagation.

The ROS of the linear fire fronts R_l did not change considerably during the lifetime of the merging fires and did not influence merging fire front development (Fig. 12). Standard deviation of R_l varied in the range 0.04–0.55 m s^{-1}.

Fig. 13 shows comparison of our results with studies of Sullivan *et al.* (2019), Viegas *et al.* (2012) and Thomas *et al.* (2017). Comparison with the null hypothesis (Eqn 2) and laboratory results of Sullivan *et al.* (2019) (Fig. 13*a*) showed that the non-dimensionless ROS R' in our experiments was greater and smaller than the null hypothesis (in contrast to Sullivan *et al.* (2019)) cosec(θ/2).

For comparison with the simplified analytical model of Viegas *et al.* (2012), we modelled our data with the Belehradek model (Ross 1993) (Fig. 13*b*). Non-linear regression with the Levenberg–Marquardt algorithm (Ranganathan 2004) was used (adj. $R^2 = 0.92$):

$$R' = 421.92 \times (\theta - 1.98)^{-1.23} \quad (3)$$

Similarly to Sullivan *et al.* (2019), we did not get agreement with Viegas *et al.* (2012). Although Viegas *et al.* (2012) conducted experiments in no-wind conditions, the R' in their study was higher than that observed in our results (Fig. 13*b*) and those of Sullivan *et al.* (2019) (Fig. 13*a*).

Comparison of dimension ROS (R_P) with the numerical simulation of Thomas *et al.* (2017) shows good agreement (Fig. 13*c*) despite different fuel types and loads.

Discussion and conclusions

The ROS of junction fire fronts is significantly different and higher than linear fire front ROS, which is consistent with other studies (Viegas *et al.* 2012, 2013; Sullivan *et al.* 2019). A greater than 60% increase in ROS was observed for junction fire fronts. However, the ROS of junction fire fronts did not change notably during the merging process (Fig. 9), in contrast to Viegas *et al.* (2012), Raposo *et al.* (2018), Thomas *et al.* (2017) and Sullivan *et al.* (2019). Previous studies (Viegas *et al.* 2013; Raposo *et al.* 2018) identified an initial acceleration phase followed by a deceleration phase for each junction fire development (Viegas *et al.* 2013; Raposo *et al.* 2018); however, our results did not show these pronounced phases for each junction fire. All fires behaved differently, having either deceleration-only, acceleration-only or both phases for all initial-angle groups. For instance, 38% of junction fire fronts showed an increase in ROS in the final stage of the merging process in contrast to Viegas *et al.* (2013 and Raposo *et al.* (2018). It is problematic for drawing any conclusion as the number of junction fires and measurement points for individual fires are limited.

We observed an increase of current angle θ in time for all initial angles (Fig. 10) except 4–14°, despite the fact the ROS of apex P did not change considerably during the merging process. Viegas *et al.* (2012) found the value of θ increases continuously, regardless of the initial configuration of the fire lines. However, the rate of increase notably differs between our studies. In the study of Viegas *et al.* (2012), the slope of the linear regression line (rate of change) decreases with increase in initial angle between two oblique fire fronts, namely 0.62, 0.16, 0.07 for 10°, 30° and 45° initial angle respectively. In our study, we observed the opposite effect: for initial angles 14°, 28–34° and 40–59°, the slope was 0.05, 0.3 and 0.3 respectively (Fig. 10). Without high-resolution measurements of radiative and convective heat transfer, it is difficult to determine why a significant increase of the

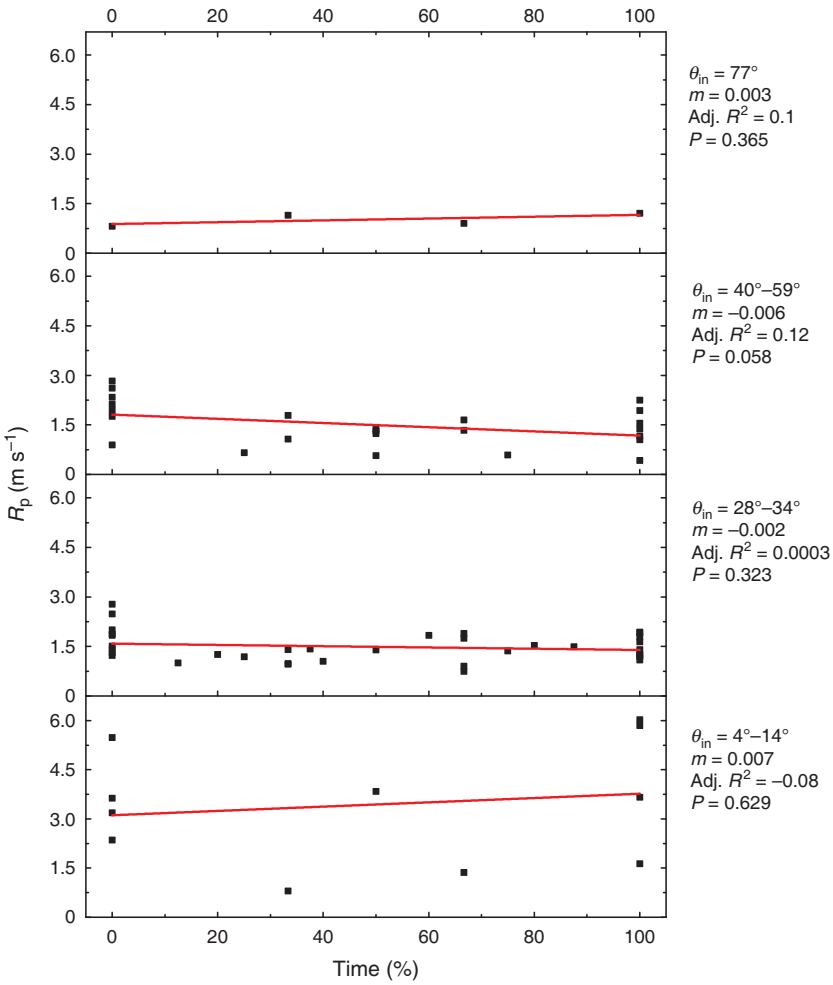

Fig. 9. Variation of the rate of spread R_P of the intersect point of two junction fire fronts. Angles in the legend indicate the value at the initial time, m is the slope of the regression line, Adj. R^2 is the adjusted R^2, P is the significance value. R_P at the 100% time step corresponds to the last time the angle between junction fire fronts became 180°.

current angle between two oblique fire fronts did not result in a significant decrease of ROS for initial angles above 28°. It should be noted that in field conditions, wind direction and speed are not constant and that resulted in asymmetry for some junction fire fronts. Asymmetry could affect the ROS and merging process in some cases.

Comparison of junction fire fronts with different length of oblique fire fronts showed no notable influence, in contrast to Sullivan *et al.* (2019) (Fig. 14). Sullivan *et al.* (2019) conducted junction fire experiments for 0.8- and 1.5-m ignition lines and found that the rates of vertex propagation in the presence of wind were consistently higher and statistically significant for 1.5 m than those for the 0.8-m ignition lines. In our study, similar ROS were observed for different junction fire front lengths (3.6–22 m) and angles. In the experiments of Sullivan *et al.* (2019), fuel was both within and outside the junction lines, providing fire spread both inward and outward. Such a fuel layout was not observed during field experiments and may be one of the reasons for the discrepancy.

Despite different trends in apex acceleration, we obtained similar results to Sullivan *et al.* (2019) for the mean ROS of junction fire fronts R_P. With increase of initial angle of junction fire fronts from 15° to 30°, 45° and 60° in Sullivan *et al.* (2019), mean ROS for 0.8-m ignition lines decreased 12.8, 37.8 and 37.8% respectively. In our study, increase from 14° to 28–34°and 40–59° resulted in a decrease of mean ROS of 38.2 and 38.2% respectively. We obtained very good qualitative agreement of mean ROS reduction for all angles, except 30°, despite different spatial scales, experiment design and fuel properties.

Analysis of video footage of merging fire fronts revealed that in all cases, junction fire fronts have a different shape to those in previous studies (Fig. 15). Different configurations of ignition lines can result in different ROS of the intersect point R_P. It is hypothesised that the left and right shoulder (Fig. 15*b*) create complex convective structures and cause changes in the ROS. In our experiments, we observed increase of the ROS in almost 40% of junction fire fronts at the final stage of merging in

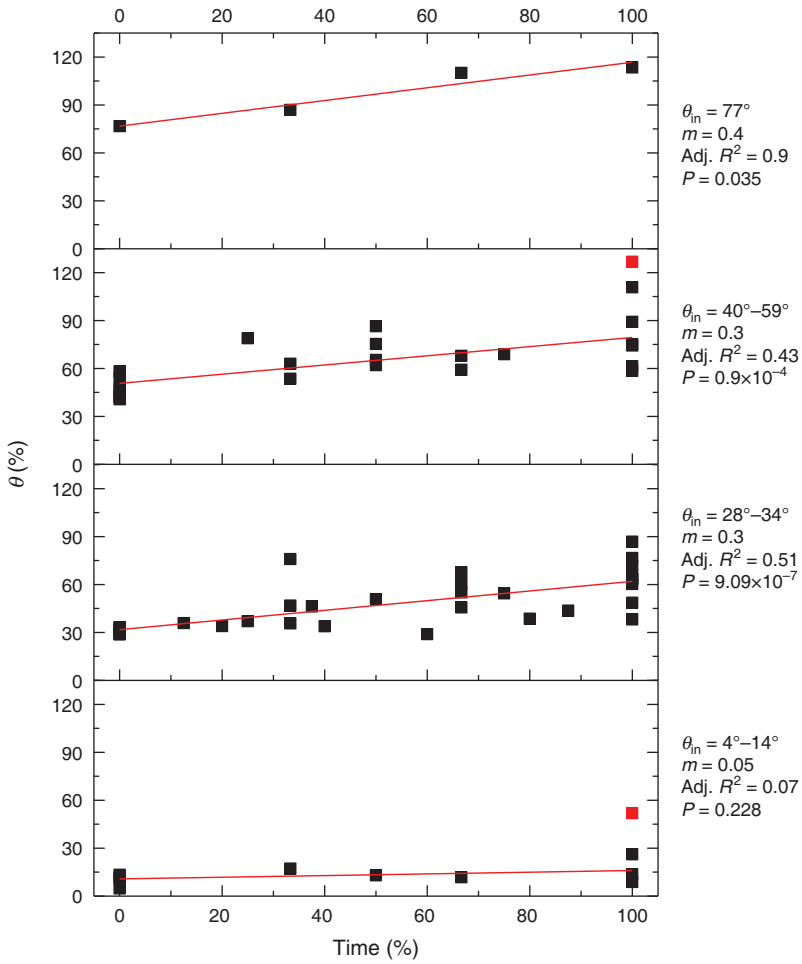

Fig. 10. Time evolution of the angle θ between junction fire fronts. Red squares represent outliers, m is the slope of the regression line, Adj. R^2 is the adjusted R^2, P is the significance value. Angles at the 100% time step correspond to the next to last value as the last value is always 180°.

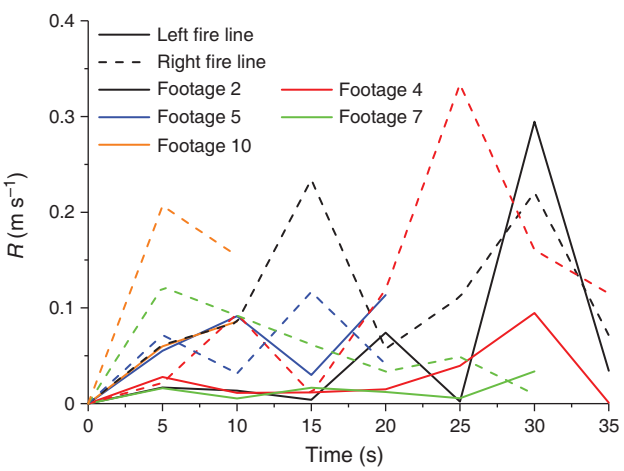

Fig. 11. Rate of spread of parallel fire fronts. Left and right fire lines are relative to direction of wind and fire front propagation.

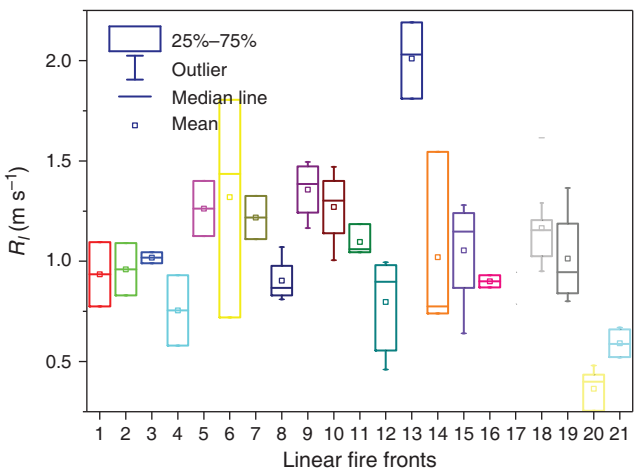

Fig. 12. Rate of spread of the linear fire fronts R_l for all tests. Colours represent individual fires.

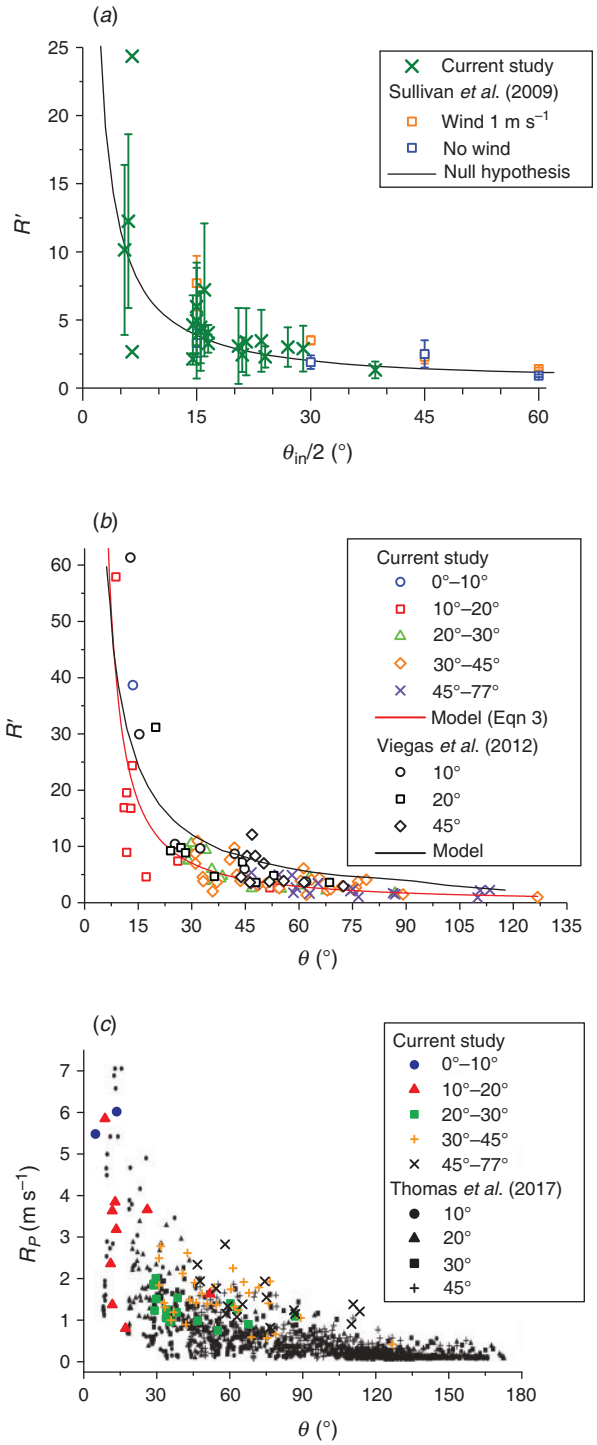

Fig. 13. Comparison with other studies: (*a*) Comparison of dimensionless rate of spread R' with study of Sullivan *et al.* (2019). Markers indicate R' for different initial angles θ_{in}. Current study represents results for wind conditions 1.8–7.0 m s^{-1}. Black line is the null hypothesis (Eqn 2). (*b*) Comparison of dimensionless rate of spread R' with Viegas *et al.* (2012). Markers indicate angle between junction fire fronts at different times. Legend shows the ranges of initial angles θ_{in}. Black line is the simplified analytical model of Viegas *et al.* (2012); red line is a regression line from current study (Eqn 3), adjusted $R^2 = 0.92$. (*c*) Comparison of the rate of spread of the intersect point of two junction fire fronts R_P with numerical results of Thomas *et al.* (2017). Markers indicate angle between junction fire fronts at different times. Legend shows the ranges of initial angles θ_{in}.

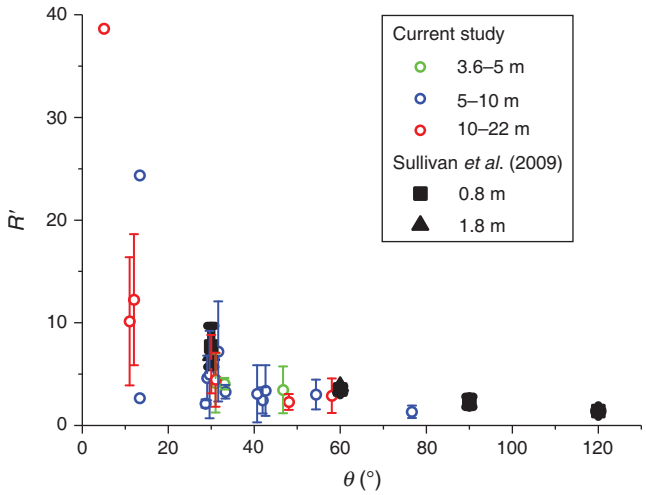

Fig. 14. Comparison of dimensionless rate of spread R' for different fire lengths with study of Sullivan *et al.* (2019).

contrast to a decrease or no change in the ROS in previous research (Viegas *et al.* 2012, 2013; Raposo *et al.* 2018; Sullivan *et al.* 2019). This configuration (Fig. 15*b*) may also prevent an increase of an angle between two fire lines for initial angles smaller than 30° and requires further investigation.

Although Sullivan *et al.* (2019) found that for the wind-driven experiments, there is an increase of the rate of propagation of the vertex above what would be expected from trigonometry alone (Eqn 2), we did not observe such an increase for all junction fire fronts. Our ROS were larger and smaller than the null hypothesis (Eqn 2) even with wind speeds of 1.8–7.0 m s^{-1}. It can be assumed that in field conditions and for wind speeds higher than 1 m s^{-1}, the R' of junction fire fronts is more complex.

The dimensionless ROS R' in our study is lower than of Viegas *et al.* (2012). The difference was up to 373%, with an average of 66% (relative to our data). A potential reason for this discrepancy could be from the way basic ROS was calculated. Viegas *et al.* (2012) calculated it without wind for a linear fire front using the same experimental conditions. In our study, we measured R_0 of the closest linear fire front in windy conditions and then corrected it to compensate for the effect of the different oblique angles. This approach allows comparisons with future experiments in different wind conditions and other studies. A similar approach was used by Sullivan *et al.* (2019). Even using the value of basic ROS found by Viegas *et al.* (2012) for straw (0.002 m s^{-1}) gives us values 30-fold higher than in their study.

Thomas *et al.* (2017) also conducted a comparison of numerical simulations (length of fire lines ~1 km) with the experimental results of Viegas *et al.* (2012) (length ~8 m). Their results showed no quantitative agreement as well. They assumed that the reason was the different scale of experiments and numerical modelling.

Fuel type and load may be have caused difference in results with Viegas *et al.* (2012) and Sullivan *et al.* (2019). Fuel in our study was a harvested wheat crop with a load of 0.11 kg m^{-2}. Viegas *et al.* (2012) used pine needle litter with a fuel load of 0.6 kg m^{-2} (six times higher) and Sullivan *et al.* (2019) used eucalypt forest fuel litter of 1.2 kg m^{-2} comprising fallen leaves, twigs and bark (10 times higher). Increasing fuel load may result in increase of the ROS owing to a significant effect on the

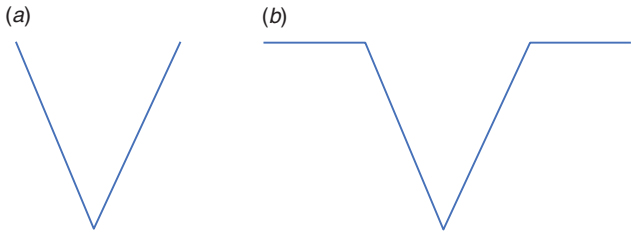

Fig. 15. Contour of junction fire fronts: (*a*) considered in all previous studies, (*b*) observed in our field experiments.

efficiency of heat transfer to unburnt fuel (Plucinski and Anderson 2008). A comparison with the numerical simulation of Thomas *et al.* (2017) shows good agreement (Fig. 13*c*) despite the fact that the fuel load in Thomas *et al.* (2017) was seven times higher and the experiments were conducted in no-wind conditions.

A decrease of fuel moisture content and air relative humidity should increase the ROS (Rossa 2017); however, a limitation of the data is that we cannot estimate these values. Neither Viegas *et al.* (2012) nor Thomas *et al.* (2017) mentioned the moisture content of the fuel bed and air relative humidity in their studies. Sullivan *et al.* (2019) indicated 3–6% fuel moisture content, at least two times lower than in our experiments (11.9%) and 30.7% relative humidity (almost 8% higher than in our experiments).

The quantification of captured video and photo imagery has traditionally been challenging and requires significant pre-experimental set up time or a complex post-processing workflow. The approach used in these experiments has the benefit of minimal set-up time (hours) with the resulting data being highly accurate across space and time. With further development and testing, it shows promise as a valuable tool for fire behaviour research, operational and management applications.

Summary

Several preliminary small- and medium-scale field experiments were conducted on harvested wheat fields to characterise fire behaviour using emerging technologies. A UAV was used to capture high-definition video imagery of fire propagation. Twenty-one junction fire fronts and five inward parallel fire fronts were identified during the experiments. Comparison between the few available studies showed considerable variation in ROS for similar conditions. These raises the following basic questions:

- Scaling. Does the size of merging fires change the ROS? The results of Raposo *et al.* (2018) (7–75 m) and our results (3.6–22 m) demonstrate that junction fire behaviour is similar at all tested scales, whereas Sullivan *et al.* (2019) showed an increase in the ROS from 0.8 to 1.8 m.
- Fuel load and structure. Do the fuel structural properties (bulk density, porosity, surface-to-volume ratio, heterogeneity, etc.) change the ROS of merging fires? We obtained similar ROS to Thomas *et al.* (2017) (grass, 7× higher fuel load), but much lower ROS than Viegas *et al.* (2012) (pine needles, 6× higher) and Sullivan *et al.* (2019) (eucalypt litter, 10× higher).
- Wind speed. How does a change in wind speed modify the ROS? We are not aware of any studies.
- Experimental design. How realistic is the V-shape contour? Our observations showed that junction fire fronts in the field always have shoulders at the top of the V, which could result in different fire behaviour compared with a 'classical' V-shape contour. This may result in acute angles and increased R' at the final stage of merging.

Existing studies on merging fires are disconnected. Future research needs to conduct experiments with similar initial conditions and measurements of convective and radiative energy. Without such data, it is not possible to draw any conclusion regarding the problems mentioned above. UAVs provide a means of improving data collection for this purpose.

Conflicts of interest

The authors declare no conflicts of interest.

Acknowledgements

This study was funded by the Bushfire and Natural Hazards Cooperative Research Centre 'Determining threshold conditions for extreme fire behaviour' project. We thank John McKinnon for providing access to his farmland for the experiments.

References

Cheney N, Gould J (1997) Fire growth and acceleration. *International Journal of Wildland Fire* **7**, 1–5. doi:10.1071/WF9970001

Cheney NP, Gould J, Anderson W (1993) The influence of fuel, weather and fire shape variables on fire-spread in grasslands. *International Journal of Wildland Fire* **3**, 31–44. doi:10.1071/WF9930031

Coen JL, Cameron M, Michalakes J, Patton EG, Riggan PJ, Yedinak KM (2013) WRF-Fire: coupled weather–wildland fire modeling with the weather research and forecasting model. *Journal of Applied Meteorology and Climatology* **52**, 16–38. doi:10.1175/JAMC-D-12-023.1

Doogan M (2006) 'The Canberra firestorm: inquests and inquiry into four deaths and four fires between 8 and 18 January 2003: Vol. I.' (ACT Magistrates Court: Canberra, ACT, Australia)

Fernández-Guisuraga JM, Sanz-Ablanedo E, Suárez-Seoane S, Calvo L (2018) Using unmanned aerial vehicles in post-fire vegetation survey campaigns through large and heterogeneous areas: opportunities and challenges. *Sensors* **18**, 586. doi:10.3390/S18020586

Filkov AI, Duff TJ, Penman TD (2018) Improving fire behaviour data obtained from wildfires. *Forests* **9**, 81. doi:10.3390/F9020081

Filkov AI, Duff TJ, Penman TD (2020*a*) Frequency of dynamic fire behaviours in Australian forest environments. *Fire* **3**, 1–19. doi:10.3390/FIRE3010001

Filkov AI, Ngo T, Matthews S, Telfer S, Penman TD (2020*b*) Impact of Australia's catastrophic 2019/20 bushfire season on communities and environment. Retrospective analysis and current trends. *Journal of Safety Science and Resilience* **1**, 44–56. doi:10.1016/J.JNLSSR.2020.06.009

Frangieh N, Morvan D, Meradji S, Accary G, Bessonov O (2018) Numerical simulation of grassland fires behavior using an implicit physical multiphase model. *Fire Safety Journal* **102**, 37–47. doi:10.1016/J.FIRESAF.2018.06.004

Hilton J, Sharples J, Sullivan A, Swedosh W (2017) Simulation of spot fire coalescence with dynamic feedback. In 'MODSIM2017: 22nd International congress on modelling and simulation', 3–8 December 2017, Hobart, Tas., Australia (Eds G Syme, D Hatton MacDonald, B Fulton, J Piantadosi) pp. 1111–1117. (Modelling and Simulation Society of Australia and New Zealand)

Hilton JE, Sullivan AL, Swedosh W, Sharples J, Thomas C (2018) Incorporating convective feedback in wildfire simulations using pyrogenic potential. *Environmental Modelling & Software* **107**, 12–24. doi:10.1016/J.ENVSOFT.2018.05.009

Hua L, Shao G (2017) The progress of operational forest fire monitoring with infrared remote sensing. *Journal of Forestry Research* **28**, 215–229. doi:10.1007/S11676-016-0361-8

Macdonald O (2017) Getting to know ArcGIS Pro. *The Cartographic Journal* **54**, 284–285. doi:10.1080/00087041.2017.1371449

Merino L, Caballero F, Martínez-de-Dios JR, Maza I, Ollero A (2012) An unmanned aircraft system for automatic forest fire monitoring and measurement. *Journal of Intelligent and Robotic Systems: Theory and Applications* **65**, 533–548. doi:10.1007/S10846-011-9560-X

Moran CJ, Seielstad CA, Cunningham MR, Hoff V, Parsons RA, Queen L, Sauerbrey K, Wallace T (2019) Deriving fire behavior metrics from UAS imagery. *Fire* **2**, 36. doi:10.3390/FIRE2020036

Morvan D, Frangieh N (2018) Wildland fires behaviour: wind effect versus Byram's convective number and consequences upon the regime of propagation. *International Journal of Wildland Fire* **27**, 636–641. doi:10.1071/WF18014

Plucinski MP, Anderson WR (2008) Laboratory determination of factors influencing successful point ignition in the litter layer of shrubland vegetation. *International Journal of Wildland Fire* **17**, 628–637. doi:10.1071/WF07046

Ranganathan A (2004) The Levenberg–Marquardt algorithm. Available at https://www.academia.edu/660131/The_levenberg_marquardt_algorithm [Verified 27 November 2020]

Raposo JR, Viegas DX, Xie X, Almeida M, Figueiredo AR, Porto L, Sharples J (2018) Analysis of the physical processes associated with junction fires at laboratory and field scales. *International Journal of Wildland Fire* **27**, 52–68. doi:10.1071/WF16173

Ross T (1993) Bělehrádek-type models. *Journal of Industrial Microbiology* **12**, 180–189. doi:10.1007/BF01584188

Rossa CG (2017) The effect of fuel moisture content on the spread rate of forest fires in the absence of wind or slope. *International Journal of Wildland Fire* **26**, 24–31. doi:10.1071/WF16049

Sullivan AL, Swedosh W, Hurley RJ, Sharples JJ, Hilton JE (2019) Investigation of the effects of interactions of intersecting oblique fire lines with and without wind in a combustion wind tunnel. *International Journal of Wildland Fire* **28**, 704–719. doi:10.1071/WF18217

Tedim F, Leone V, Amraoui M, Bouillon C, Coughlan RM, Delogu MG, Fernandes MP, Ferreira C, McCaffrey S, McGee KT, Parente J, Paton D, Pereira GM, Ribeiro ML, Viegas DX, Xanthopoulos G (2018) Defining extreme wildfire events: difficulties, challenges, and impacts. *Fire* **1**, 9. doi:10.3390/FIRE1010009

Thomas CM, Sharples JJ, Evans JP (2017) Modelling the dynamic behaviour of junction fires with a coupled atmosphere–fire model. *International Journal of Wildland Fire* **26**, 331–344. doi:10.1071/WF16079

Viegas DX (2012) Extreme fire behaviour. In 'Forest management: technology, practices and impact.' (Eds ACB Cruz, REG Correia) pp. 1–56 (Nova Science Publishers, Inc.: New York, NY, USA)

Viegas DX, Raposo JR, Davim DA, Rossa CG (2012) Study of the jump fire produced by the interaction of two oblique fire fronts. Part 1. Analytical model and validation with no-slope laboratory experiments. *International Journal of Wildland Fire* **21**, 843–856. doi:10.1071/WF10155

Viegas DX, Raposo J, Figueiredo A (2013) Preliminary analysis of slope and fuel bed effect on jump behavior in forest fires. *Procedia Engineering* **62**, 1032–1039. doi:10.1016/J.PROENG.2013.08.158

Williams J, Hamilton L (2005) The mega-fire phenomenon: toward a more effective management model. A concept paper. Brookings Institution. (Washington, DC, USA) Available at http://www.bushfirecrc.com/sites/default/files/managed/resource/mega-fire_concept_paper_september_20_ 2005.pdf [Verified 9 September 2019]

Appendix 1

Table A1. Evolution of junction fire fronts in time

R_P is the rate of spread of the intersect point of two junction fire fronts (m s^{-1}); R_I is the rate of spread of a linear fire front (m s^{-1}), s.d. is the standard deviation (m s^{-1}), θ is the current angle between two junction fire fronts (°)

ID	Footage no.	Fire no.	Time (s)	R_I (m s^{-1})	Mean R_I (m s^{-1})	s.d. (m s^{-1})	R_P (m s^{-1})	Mean R_P (m s^{-1})	s.d. (m s^{-1})	θ (°)
1	1	1	0							47
2	1	1	2	1.10	0.94	0.23	2.14	1.71	0.61	111
3	1	1	4	0.78			1.28			180
4	1	2	0							33
5	1	2	2	1.09	0.96	0.18	1.39	1.66	0.38	77
6	1	2	4	0.83			1.93			180
7	1	3	0							31
8	1	3	2	0.99	1.02	0.04	1.84	1.82	0.03	72
9	1	3	4	1.05			1.80			180
10	1	4	0							32
11	1	4	2	0.93	0.76	0.25	2.78	2.02	1.08	63
12	1	4	4	0.58			1.25			180
13	1	5	0							13
14	1	5	2	1.13	1.26	0.19	3.21	2.47	1.04	52
15	1	5	4	1.40			1.73			180
16	1	6	0							43
17	1	6	2	1.44	1.32	0.26	2.59	2.03	0.67	62
18	1	6	4	1.81			1.29			61
19	1	6	6	0.72			2.20			180
20	3	1	0							5
21	3	7	2	1.11	1.22	0.15	5.42	5.71	0.42	14
22	3	7	4	1.33			6.01			180
23	3	8	0							31
24	3	8	2	1.07	0.90	0.11	2.50	1.86	0.48	76
25	3	8	4	0.85			1.36			60
26	3	8	6	0.89			1.69			66
27	3	8	8	0.81			1.86			180
28	3	9	0							11
29	3	9	2	1.45	1.36	0.15	2.35	2.58	2.26	17
30	3	9	4	1.17			0.79			12
31	3	9	6	1.50			1.36			9
32	3	9	8	1.32			5.83			180
33	4	10	0							48
34	4	10	2	1.47	1.27	0.19	2.01	1.40	0.41	63
35	4	10	4	1.28			1.09			59
36	4	10	6	1.01			1.33			58
37	4	10	8	1.33			1.18			180
38	6	11	0							58
39	6	11	2	1.19	1.10	0.08	2.72	1.80	0.81	86
40	6	11	4	1.06			1.18			75
41	6	11	6	1.05			1.50			180
42	7	12	0							30
43	7	12	2	0.56	0.80	0.23	1.48	1.36	0.30	34
44	7	12	4	0.46			1.22			34
45	7	12	6	0.95			0.96			29
46	7	12	8	1.00			1.83			39
47	7	12	10	0.98			1.47			38
48	7	12	12	0.85			1.19			180
49	9	13	0							12
50	9	13	2	1.81	2.01	0.19	3.65	3.74	0.16	13
51	9	13	4	2.03			3.92			26
52	9	13	6	2.19			3.66			180
53	10	14	0							54

(*Continued*)

Table A1. (Continued)

ID	Footage no.	Fire no.	Time (s)	R_I (m s^{-1})	Mean R_I (m s^{-1})	s.d. (m s^{-1})	R_P (m s^{-1})	Mean R_P (m s^{-1})	s.d. (m s^{-1})	θ (°)
54	10	14	2	0.78	1.02	0.46	1.73	1.67	0.28	65
55	10	14	4	0.74			1.37			74
56	10	14	6	1.55			1.92			180
57	10	15	0							77
58	10	15	2	1.28	1.05	0.29	0.84	1.02	0.18	87
59	10	15	4	1.10			1.15			110
60	10	15	6	1.20			0.88			113
61	10	15	8	0.64			1.19			180
62	13	16	0							30
63	13	16	2	0.87	0.90	0.04	2.03	1.71	0.45	60
64	13	16	4	0.93			1.39			180
65	13	17	0							29
66	13	17	2	0.81	0.87	0.10	1.87	1.22	0.44	47
67	13	17	4	0.97			1.01			68
68	13	17	6	0.76			0.90			87
69	13	17	8	0.92			1.09			180
70	13	18	0							33
71	13	18	2	1.20	1.17	0.20	1.32	1.43	0.26	36
72	13	18	4	1.62			1.01			37
73	13	18	6	1.03			1.24			46
74	13	18	8	1.01			1.41			51
75	13	18	10	0.95			1.39			46
76	13	18	12	1.21			1.94			54
77	13	18	14	1.16			1.37			44
78	13	18	16	1.04			1.53			49
79	13	18	18	1.29			1.64			180
80	13	19	0							41
81	13	19	2	0.80	1.01	0.25	2.13	1.64	0.47	54
82	13	19	4	0.88			1.81			68
83	13	19	6	1.37			1.60			89
84	13	19	8	1.01			1.02			180
85	16	20	0							42
86	16	20	2	0.26	0.37	0.10	0.91	0.63	0.18	79
87	16	20	4	0.26			0.66			75
88	16	20	6	0.40			0.57			69
89	16	20	8	0.44			0.60			127
90	16	20	10	0.48			0.42			180
91	16	21	0							29
92	16	21	2	0.65	0.59	0.08	1.24	1.04	0.23	36
93	16	21	4	0.53			0.95			55
94	16	21	6	0.67			0.75			63
95	16	21	8	0.52			1.22			180

Table A2. Evolution of parallel fire fronts in time

V_{left} is the ROS of the left fire front (m s^{-1}), V_{right} is the ROS of the right fire front (m s^{-1}), R_I is the rate of spread of a linear fire front (m s^{-1}), s.d. is the standard deviation (m s^{-1})

Footage no.	Time (s)	V_{left} (m s^{-1})	V_{right} (m s^{-1})	R_I (m s^{-1})
2	5	0.02	0.06	1.16
2	10	0.01	0.08	1.57
2	15	0.00	0.23	1.23
2	20	0.07	0.06	0.94
2	25	0.00	0.11	1.32
2	30	0.29	0.22	1.14
2	35	0.03	0.07	1.36
Mean (m s^{-1})		0.06	0.12	1.25
s.d. (m s^{-1})		0.53	0.38	0.20
4	5	0.03	0.02	0.96
4	10	0.01	0.09	1.12
4	15	0.01	0.01	1.13
4	20	0.01	0.12	1.10
4	25	0.04	0.33	1.22
4	30	0.09	0.16	1.08
4	35	0.00	0.12	1.34
Mean (m s^{-1})		0.03	0.12	1.14
s.d. (m s^{-1})		0.16	0.54	0.12
5	5	0.06	0.07	1.07
5	10	0.09	0.03	1.16
5	15	0.03	0.12	1.69
5	20	0.11	0.04	1.52
Mean (m s^{-1})		0.07	0.07	1.36
s.d. (m s^{-1})		0.19	0.19	0.30
7	5	0.02	0.12	1.01
7	10	0.01	0.09	1.09
7	15	0.02	0.06	1.42
7	20	0.01	0.03	1.56
7	25	0.01	0.05	2.29
7	30	0.03	0.01	1.77
Mean (m s^{-1})		0.01	0.06	1.52
s.d. (m s^{-1})		0.05	0.20	0.47
10	5	0.06	0.21	1.96
10	10	0.09	0.15	1.58
Mean (m s^{-1})		0.07	0.18	1.77
s.d. (m s^{-1})		0.09	0.19	0.27

Table A3. Spatial locations and dimensions of junction fire fronts

$P(x,–)$ is the x coordinate of intersect point P of two junction fire fronts; $P(–,y)$ is the y coordinate of intersect point P of two junction fire fronts; a is the maximum distance between the junction fire fronts and b, c are the lengths of the junction fire fronts (Fig. 1*b*); d is the distance travelled of intersect point P. Projected coordinate system is GDA 1994 VICGRID94 and projection is Lambert Conformal Conic

ID	Footage no.	Fire no.	Time (s)	$P(x,–)$	$P(–,y)$	a (m)	b (m)	c (m)	d (m)
1	1	1	0	2409794.026	2456079.359	3.6	4.2	4.8	
2	1	1	2	2409793.871	2456075.075	4.2	2.7	2.4	4.29
3	1	1	4	2409793.91	2456072.505				2.57
4	1	2	0	2409772.841	2456083.08	3.2	5.5	3.6	
5	1	2	2	2409772.458	2456080.33	4.2	4.1	2.1	2.78
6	1	2	4	2409771.893	2456076.517				3.85
7	1	3	0	2409785.081	2456080.476	2.9	5.6	4.8	
8	1	3	2	2409784.235	2456076.898	3.8	3.1	3.4	3.68
9	1	3	4	2409783.411	2456073.398				3.60
10	1	4	0	2409805.545	2456069.703	3.8	6.9	6.9	
11	1	4	2	2409803.543	2456064.514	4.3	3.4	4.5	5.56
12	1	4	4	2409802.746	2456062.141				2.50
13	1	5	0	2409799.299	2456072.363	2.0	7.9	6.9	
14	1	5	2	2409798.958	2456065.958	3.1	3.9	2.4	6.41
15	1	5	4	2409798.46	2456062.536				3.46
16	1	6	0	2409778.273	2456081.455	9.2	13.4	8.8	
17	1	6	2	2409776.681	2456076.52	5.9	6.0	5.3	5.19
18	1	6	4	2409776.329	2456073.97	5.2	5.3	4.9	2.57
19	1	6	6	2409775.539	2456069.645				4.40
20	3	1	0	2409751.744	2456193.357	2.2	18.9	17.3	
21	3	7	2	2409748.897	2456182.907	2.3	9.9	9.9	10.83
22	3	7	4	2409746.712	2456171.083				12.02
23	3	8	0	2409777.27	2456182.61	6.3	11.7	11.8	
24	3	8	2	2409777.115	2456177.602	5.8	4.4	5.0	5.01
25	3	8	4	2409777.084	2456174.88	5.4	5.4	5.3	2.72
26	3	8	6	2409776.964	2456171.498	5.9	5.4	5.5	3.38
27	3	8	8	2409777.317	2456167.784				3.73
28	3	9	0	2409734.743	2456176.291	4.1	17.4	19.4	
29	3	9	2	2409733.253	2456171.828	2.2	7.3	7.1	4.71
30	3	9	4	2409732.794	2456170.306	1.5	7.2	7.0	1.59
31	3	9	6	2409732.186	2456167.649	1.2	7.7	7.8	2.73
32	3	9	8	2409730.209	2456156.159				11.66
33	4	10	0	2409951.124	2456139.131	9.4	12.1	10.8	
34	4	10	2	2409950.893	2456135.123	8.2	8.0	7.6	4.01
35	4	10	4	2409950.614	2456132.954	7.8	8.1	7.8	2.19
36	4	10	6	2409950.21	2456130.328	9.1	8.2	10.1	2.66
37	4	10	8	2409950.063	2456127.973				2.36
38	6	11	0	2409822.975	2456389.433	9.6	7.8	11.1	
39	6	11	2	2409825.803	2456384.794	9.1	4.1	8.4	5.43
40	6	11	4	2409826.773	2456382.643	10.3	6.4	10.0	2.36
41	6	11	6	2409827.853	2456379.834				3.01
42	7	12	0	2409974.566	2456343.383	11.4	15.3	21.7	
43	7	12	2	2409975.385	2456340.535	3.3	5.1	5.9	2.96
44	7	12	4	2409976.501	2456338.37	3.7	5.6	6.7	2.44
45	7	12	6	2409977.445	2456336.694	2.9	5.6	6.0	1.92
46	7	12	8	2409978.965	2456333.357	3.2	4.7	5.1	3.67
47	7	12	10	2409979.914	2456330.566	3.2	4.0	5.1	2.95
48	7	12	12	2409980.535	2456328.271				2.38
49	9	13	0	2409379.365	2456399.299	4.4	19.7	21.2	
50	9	13	2	2409380.027	2456392.032	2.2	9.9	10.0	7.30
51	9	13	4	2409381.564	2456384.337	2.1	4.7	4.4	7.85
52	9	13	6	2409382.445	2456377.075				7.32
53	10	14	0	2409626.11	2456485.547	6.3	5.0	7.7	
54	10	14	2	2409628.753	2456483.305	4.2	3.6	4.1	3.47
55	10	14	4	2409630.8	2456481.482	5.2	5.0	3.5	2.74
56	10	14	6	2409633.256	2456478.542				3.83

(*Continued*)

Table A3. (Continued)

ID	Footage no.	Fire no.	Time (s)	$P(x,-)$	$P(-,y)$	a (m)	b (m)	c (m)	d (m)
57	10	15	0	2409620.085	2456468.456	8.5	7.6	6.0	
58	10	15	2	2409621.326	2456467.338	5.1	3.9	3.5	1.67
59	10	15	4	2409622.967	2456465.719	8.6	5.8	4.7	2.31
60	10	15	6	2409624.261	2456464.513	8.3	6.4	3.3	1.77
61	10	15	8	2409625.892	2456462.772				2.39
62	13	16	0	2409358.657	2456570.242	3.6	5.5	7.1	
63	13	16	2	2409358.615	2456566.177	3.7	2.5	4.3	4.07
64	13	16	4	2409357.95	2456563.471				2.79
65	13	17	0	2409353.327	2456571.078	3.0	6.1	6.1	
66	13	17	2	2409353.77	2456567.371	2.4	2.8	3.1	3.73
67	13	17	4	2409354.189	2456565.385	3.7	3.8	2.3	2.03
68	13	17	6	2409354.486	2456563.608	6.2	4.1	4.9	1.80
69	13	17	8	2409354.835	2456561.461				2.17
70	13	18	0	2409378.397	2456564.334	4.7	8.2	8.1	
71	13	18	2	2409377.883	2456561.752	2.8	4.5	4.6	2.63
72	13	18	4	2409377.49	2456559.778	2.7	4.1	4.5	2.01
73	13	18	6	2409377.142	2456557.327	4.8	5.2	6.6	2.48
74	13	18	8	2409377.385	2456554.526	5.7	6.1	7.0	2.81
75	13	18	10	2409377.785	2456551.768	4.8	5.6	6.6	2.79
76	13	18	12	2409378.562	2456547.961	5.2	5.0	6.1	3.89
77	13	18	14	2409379.094	2456545.269	4.3	5.7	5.9	2.74
78	13	18	16	2409379.425	2456542.227	4.0	4.5	5.1	3.06
79	13	18	18	2409379.822	2456538.978				3.27
80	13	19	0	2409390.856	2456555.397	5.7	8.4	8.1	
81	13	19	2	2409391.162	2456551.148	5.1	5.7	5.6	4.26
82	13	19	4	2409391.4	2456547.54	4.6	4.2	4.0	3.62
83	13	19	6	2409391.232	2456544.352	4.3	3.0	3.0	3.19
84	13	19	8	2409391.467	2456542.327				2.04
85	16	20	0	2409399.934	2456593.597	4.0	4.3	5.9	
86	16	20	2	2409399.772	2456591.791	2.7	1.8	2.3	1.81
87	16	20	4	2409399.73	2456590.479	2.9	1.8	2.8	1.31
88	16	20	6	2409399.568	2456589.344	3.3	1.8	3.4	1.15
89	16	20	8	2409399.35	2456588.161	3.3	1.2	2.4	1.20
90	16	20	10	2409399.231	2456587.329				0.84
91	16	21	0	2409343.948	2456604.823	4.3	8.5	6.4	
92	16	21	2	2409343.903	2456602.346	2.8	4.8	3.8	2.48
93	16	21	4	2409343.96	2456600.454	3.6	4.3	3.1	1.89
94	16	21	6	2409343.598	2456599.001	3.2	3.6	2.0	1.50
95	16	21	8	2409343.622	2456596.562				2.44

Table A4. Spatial locations of plots and ignition lines

Plots and ignition lines are defined in Fig. 2*b*. Points outline boundaries of plots and ends of ignition lines. (x,–) is the x coordinate and (–,y) is the y coordinate of points. Projected coordinate system is GDA 1994 VICGRID94 and projection is Lambert Conformal Conic

Object type	Point no.	(x,–)	(–,y)
Plot 1	1	2409665.425	2456382.905
Plot 1	2	2409711.18	2456373.805
Plot 1	3	2409726.796	2456414.464
Plot 1	4	2410063.414	2456365.783
Plot 1	5	2410022.582	2455972.233
Plot 1	6	2409620.419	2456030.614
Plot 2	1	2409154.218	2456643.835
Plot 2	2	2409545.89	2456598.162
Plot 2	3	2409563.208	2456558.566
Plot 2	4	2409661.377	2456547.207
Plot 2	5	2409624.519	2456223.836
Plot 2	6	2409325.489	2456262.977
IL1	1	2409642.848	2456104.404
IL1	2	2410017.097	2456041.64
IL2	1	2409654.462	2456209.864
IL2	2	2410027.764	2456155.069
IL3	1	2409730.171	2456407.105
IL3	2	2410056.394	2456357.696
IL4	1	2409262.77	2456445.999
IL4	2	2409614.617	2456364.246
IL5	1	2409203.242	2456596.406
IL5	2	2409644.464	2456538.751
IL6	1	2409174.886	2456636.524
IL6	2	2409531.391	2456590.547